JACS
JOURNAL OF THE AMERICAN CHEMICAL SOCIETY
pubs.acs.org/JACS
Article

High-Throughput Study of Antisolvents on the Stability of Multicomponent Metal Halide Perovskites through Robotics-Based Synthesis and Machine Learning Approaches

Kate Higgins, Maxim Ziatdinov, Sergei V. Kalinin, and Mahshid Ahmadi*

Cite This: J. Am. Chem. Soc. 2021, 143, 19945−19955

ABSTRACT: Antisolvent crystallization methods are frequently used to fabricate high-quality metal halide perovskite (MHP) thin films, to produce sizable single crystals, and to synthesize nanoparticles at room temperature. However, a systematic exploration of the effect of specific antisolvents on the intrinsic stability of multicomponent MHPs has yet to be demonstrated. Here, we develop a high-throughput experimental workflow that incorporates chemical robotic synthesis, automated characterization, and machine learning techniques to explore how the choice of antisolvent affects the intrinsic stability of binary MHP systems in ambient conditions over time. Different combinations of the end-members, $MAPbI_3$, $MAPbBr_3$, $FAPbI_3$, $FAPbBr_3$, $CsPbI_3$, and $CsPbBr_3$ (MA, methylammonium; FA^+, formamidinium), are used to synthesize 15 combinatorial libraries, each with 96 unique combinations. In total, roughly 1100 different compositions are synthesized. Each library is fabricated twice by using two different antisolvents: toluene and chloroform. Once synthesized, photoluminescence spectroscopy is automatically performed every 5 min for approximately 6 h. Nonnegative matrix factorization (NMF) is then utilized to map the time- and compositional-dependent optoelectronic properties. Through the utilization of this workflow for each library, we demonstrate that the selection of antisolvent is critical to the intrinsic stability of MHPs in ambient conditions. We explore possible dynamical processes, such as halide segregation, responsible for either the stability or eventual degradation as caused by the choice of antisolvent. Overall, this high-throughput study demonstrates the vital role that antisolvents play in the synthesis of high-quality multicomponent MHP systems.

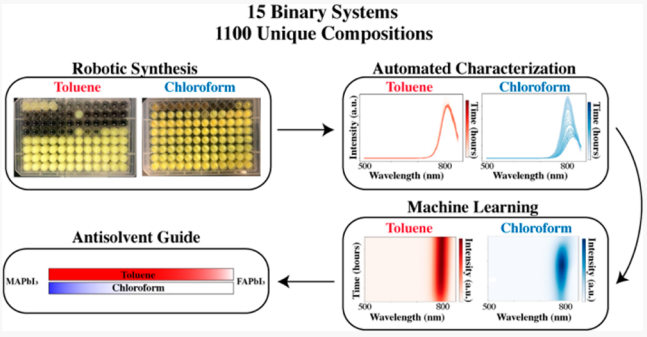

INTRODUCTION

Considerable research attention has focused on metal halide perovskites (MHPs) over recent years because of the combination of exceptional optoelectronic properties and low fabrication cost, making them ideal candidates for a variety of applications, such as solar cells,[1] photodetectors,[2] ionizing radiation sensors,[3,4] and light-emitting diodes.[5,6] Even so, the development of MHPs for commercialization must overcome an obstacle, namely stability in the pure or device-integrated form.[7,8] Overcoming adverse effects stemming from external stimuli can be minimized or avoided by utilizing established encapsulation techniques and device engineering.[9−11] Simultaneously, another strategy is to improve the intrinsic stability by cation and/or halide alloying to synthesize multicomponent MHPs.[12−14] A multitude of studies have demonstrated how the incorporation of other cations, particularly cesium (Cs^+)[15] and formamidinium (FA^+)[16] into methylammonium (MA) systems, leads to improved stability in ambient and operational conditions. Mixing halides, such as bromine (Br^-),[17] iodide (I^-), and chlorine (Cl^-),[13] has also proven to be an effective strategy toward stable perovskite materials.

Antisolvent crystallization is an efficient solution-based method to produce high-quality perovskite thin films, to synthesize high-quality single crystals,[18] and to fabricate nanoparticles at room temperature.[19] Simply, this approach requires the rapid application of the antisolvent to a perovskite solution, and the antisolvent then extracts the solvent, leading to the fast supersaturation of the perovskite precursor and subsequent precipitation. Many studies have focused on the investigation of antisolvents, including the types, volumes, and the mixture of solvents.[20] For example, Sakai et al. demonstrated that dropping toluene on the perovskite precursor deposited film during spin-coating can enhance the early stages of nucleation and grain growth, depending on the chemical composition of the precursor solution.[21] Wang et al. postulated that the use of chlorobenzene mixed with isopropyl

Received: September 22, 2021
Published: November 18, 2021

https://doi.org/10.1021/jacs.1c10045
J. Am. Chem. Soc. 2021, 143, 19945−19955

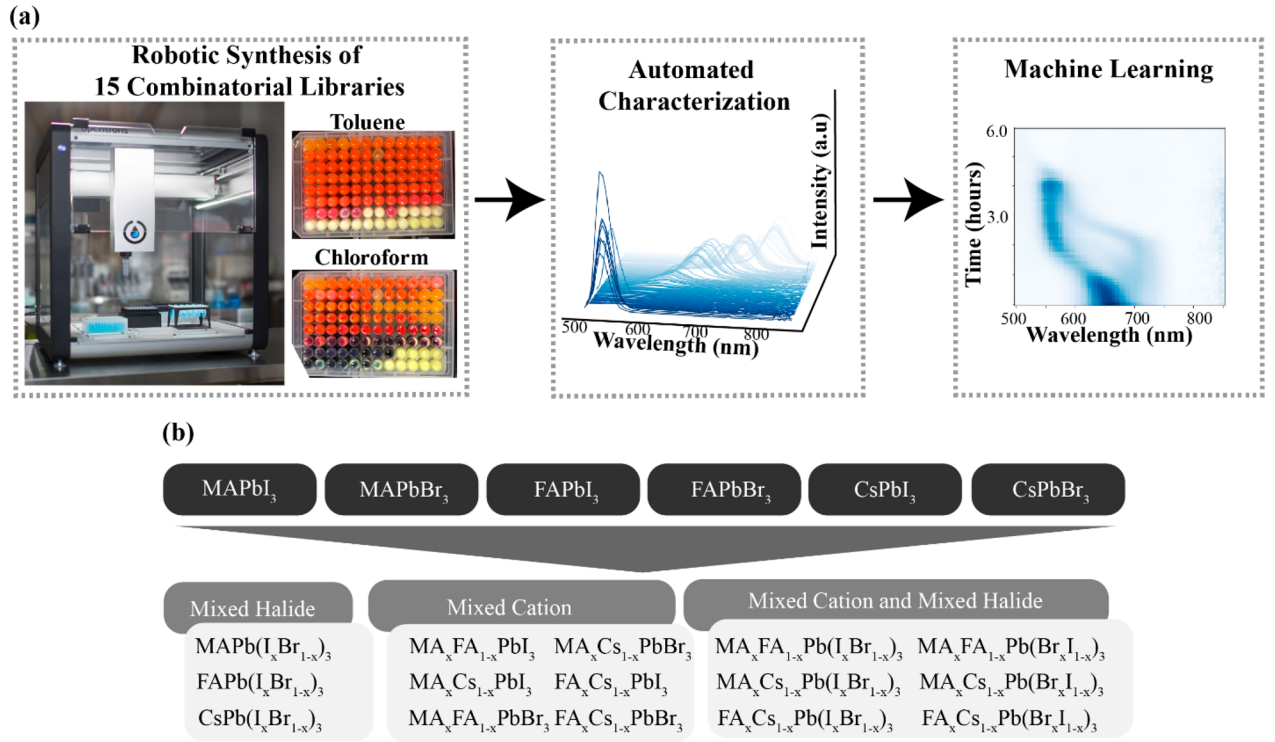

Figure 1. (a) Schematic of the experimental workflow utilized for the exploration of 15 combinatorial libraries of MHPs. We utilize robotic synthesis to fabricate a library twice with two different antisolvents: toluene and chloroform. Photoluminescence (PL) spectroscopy is automatically performed next. Finally, we utilize machine learning to effectively map characteristic PL behaviors onto composition regions. (b) List of all combinatorial libraries that were chosen from combinations of the six end-members.

alcohol removes residual chlorobenzene, therefore increasing the grain size of the perovskite film and drop in defect density.[22]

To date, much of these investigations have utilized manual trial-and-error approaches to decide which antisolvent is applicable for a particular perovskite system. Recently, automated experimentation has proven to accelerate this trial-and-error process through synthesis[23−26] and full device preparation workflows.[27,28] We have also previously reported the development of a workflow for materials discovery utilizing both automated synthesis and machine learning.[29] However, the number of groups utilizing these workflows to explore antisolvent engineering is small. Gu et al. utilized a robot-based high-throughput workflow to screen antisolvents on single-component MHPs.[24] By testing 48 different organic ligands as antisolvents and three commonly used solvents—dimethyl sulfoxide (DMSO), γ-butyrolactone (GBL), and *N*,*N*-dimethylformamide (DMF)—they explored how the choice of solvent and antisolvent affects the formation of microcrystals. As shown in another high-throughput study screening antisolvents by Manion et al., the quality of thin films can be predicted by analyzing these formations.[30] While both high-throughput studies focus on the effect of antisolvents on single end-member systems, studies exploring the effect of antisolvent engineering on multicomponent MHP systems is limited, and none have explored the intrinsic stability of these binary systems in ambient conditions. Determining the intrinsic stability of a composition is a crucial step in developing a stable and efficient device for applications.

Here, we utilize our previously reported workflow[29] to explore how the choice of antisolvent affects the photoluminescent (PL) behavior, and therefore stability, of multi-component MHPs over time in ambient conditions. With the use of a pipetting robot, we synthesize 15 different binary perovskite systems, also referred to as a combinatorial library, twice utilizing two different solvents: toluene and chloroform. Overall, roughly 1100 unique perovskite compositions were synthesized. Next, photoluminescence (PL) spectroscopy is performed on each combinatorial library in ambient conditions for approximately 6 h. Finally, through the incorporation of multivariate statistical analysis, specifically nonnegative matrix factorization (NMF), we map the time- and compositional-dependent PL behavior of each combinatorial library. Through the usage of this workflow for each combinatorial library, we characterize the intrinsic stability for each system in a specific antisolvent, helping guide future experiments done elsewhere.

RESULTS AND DISCUSSION

We utilize a workflow[29] established by our group for the rapid synthesis and characterization of MHPs that combines combinatorial synthesis and rapid throughput PL measurements. Further, we adopt a multivariate statistical analysis to explore the variability of the optical band gap and PL properties over time across the compositional space. A schematic of the workflow used is shown in Figure 1a.

In this study, we explore 15 different multicomponent MHP binary systems as shown in Figure 1b. Our chosen end-members are $MAPbI_3$, $MAPbBr_3$, $FAPbI_3$, $FAPbBr_3$, $CsPbI_3$, and $CsPbBr_3$. Synthesis details of the end-member solutions are provided in the Supporting Information and Tables S1 and S2. We chose common solvents for each end-member, such as dimethyl sulfoxide (DMSO), γ-butyrolactone (GBL), and *N*,*N*-dimethylformamide (DMF), to dissolve each precursor. In each combinatorial library, there are 96 unique

https://doi.org/10.1021/jacs.1c10045
J. Am. Chem. Soc. 2021, 143, 19945−19955

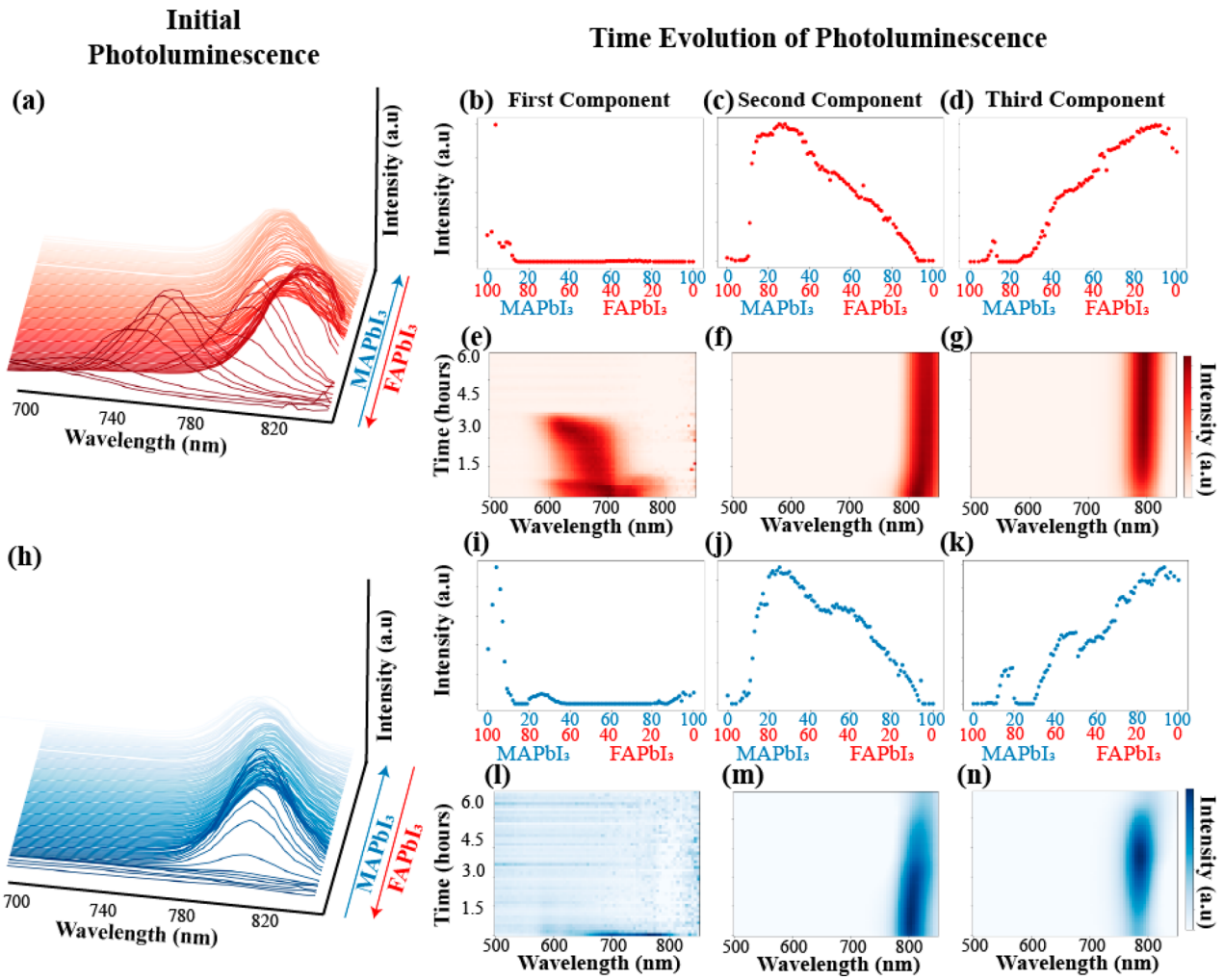

Figure 2. Double cation lead iodide system, $MA_xFA_{1-x}PbI_3$. (a) Initial PL behavior when toluene is used as the antisolvent. (b–d) Loading maps for (b) $FAPbI_3$-rich compositions, (c) solid solutions of $FAPbI_3$ and $MAPbI_3$, and (d) $MAPbI_3$-rich compositions, respectively. (e–g) Characteristic PL behaviors for (e) $FAPbI_3$-rich compositions, (f) solid solutions of $FAPbI_3$ and $MAPbI_3$, and (g) $MAPbI_3$-rich compositions, respectively. (h) Initial PL behavior when chloroform is used as the antisolvent. Similar to NMF decomposition for the toluene data set (i–k) and (l–n) are the (i, j, k) loading maps and (l, m, n) characteristic PL behaviors for $FAPbI_3$-rich compositions, solid solutions of $FAPbI_3$ and $MAPbI_3$, and $MAPbI_3$-rich compositions, respectively.

compositions, meaning that roughly 1100 unique compositions were synthesized. We then utilize an antisolvent approach to precipitate microcrystals.[4,31] Commonly used antisolvents documented by other works are classified into two categories: halogenated (chlorobenzene[32] and chloroform[31]) and non-halogenated (toluene,[17] anisole,[33] diethyl ether,[34] and ethyl acetate[35]). Here, we chose to utilize two antisolvents, chloroform and toluene, as they represent each category and because these antisolvents are heavily used in the production of high-quality MHPs. Because we use two antisolvents, each combinatorial library is synthesized twice, and therefore, in this study, roughly 2880 different microcrystal samples in total were synthesized and characterized, only taking approximately 270 h.

First, utilizing a programmable pipetting robot (Opentrons; https://opentrons.com/) and employing classical 96-well microplates, we create the combinatorial libraries. We control the composition of each well by programming the robot to pipet the desired quantity of the end-member solution. After the deposition of the end-member solutions, the antisolvent is pipetted into each well. The formation of microcrystals is apparent by the color change that occurs immediately upon the addition of the antisolvent. For this study, we selected a fine grid of data points with each composition only being 1 or 2% different because we did not utilize an iterative approach in this study since noticeable differences in PL behavior occur with small compositional changes. Details of the synthesis and photographs of selected microplates are provided in the Supporting Information (Figure S1).

To characterize composition-dependent optoelectronic properties, we utilize an automated multimode well plate reader with the capability to perform photoluminescence spectroscopy. Details of these measurements are provided in the Supporting Information. By studying the evolution of optical properties, we extract information regarding dynamical processes related to MHP formation, ionic movement, phase changes, and degradation[36–38] to characterize the intrinsic stability of MHPs in ambient condition. While other common methods, such as X-ray diffraction (XRD)[38,39] and UV–vis absorption spectroscopy,[36,40] can also be used to explore the intrinsic stability of MHPs, here, we utilize PL spectroscopy because it can be easily incorporated into automated

https://doi.org/10.1021/jacs.1c10045
J. Am. Chem. Soc. 2021, 143, 19945–19955

workflows. We can measure the PL spectra of 96 compositions in roughly 5 min. We repeat this measurement for approximately 6 h to obtain a time- and composition-dependent data set for each combinatorial library.

To effectively map the time- and composition-dependent PL properties and stability relationships concurrently, we adopt a multivariate statistical approach, in particular, nonnegative matrix factorization (NMF).[29] NMF also allows for the efficient extrapolation of material properties or chemical reactions with large data sets, such as a large number of compositions or measurements. Here, the entire data set, $L(x,y,\lambda,t)$, is analyzed via the decomposition

$$L(x, y, \lambda, t) = \sum_{i=1}^{N} L_i(x, y)\, g_i(\lambda, t)$$

where $L_i(x,y)$ are the loading maps, representing the variability in PL behavior across the compositional space, and $g_i(\lambda,t)$ are the end-members that determine characteristic behaviors in the time-spectral domain. Here, the loading maps are a 1D plot in which the x-axis represents compositional change and the y-axis is the intensity, indicating if the end-member applies to the composition; i.e., low intensity, the end-member is less applicable. End-member maps are 2D plots, demonstrating how the characteristic PL behavior changes over time. For a majority of the binary systems, three components ($N = 3$) were chosen by visual inspection as it most accurately describes each binary system. We provide a more in-depth discussion of this selection process in the Supporting Information and Figure S2. Overall, the utilization of NMF here allows for visual description of PL behavior evolution of broad compositional regions of each system. The evolution of PL behavior provides insight into the intrinsic stability of these compositional regions. A composition is defined qualitatively stable if we do not observe the formation of secondary peaks, shifts in peak positions, or the complete disappearance of the peak as these changes indicate complex, dynamical processes, such as halide segregation, phase separation, or degradation.

As mentioned previously, the effect of an individual antisolvent, either toluene or chloroform, for crystallization was explored by characterizing a total of 15 combinatorial libraries, each containing 96 unique compositions. For each plate, we have a time- and composition-dependent data set by automatically measuring the PL over time. Both the data files and code utilized for this study are posted publicly on GitHub (https://git.io/JCLC7). While all combinatorial libraries are fully explored in the Supporting Information (Figures S3–S17), here, we focus on only four combinatorial libraries: a mixed cation system, $MA_xFA_{1-x}PbI_3$, a mixed halide system, $MAPb(I_xBr_{1-x})_3$, and two mixed cation and mixed halide systems, $MA_xCs_{1-x}Pb(I_xBr_{1-x})_3$ and $MA_xCs_{1-x}Pb(Br_xI_{1-x})_3$.

First, we begin with the exploration of the initial PL behavior of the mixed cation system, $MA_xFA_{1-x}PbI_3$, as shown in Figure 2a,h. Regardless of the antisolvent used, we observe the shifting of the PL peak as the alloying increases, confirming compositional tuning of the band gap.[41] Noticeably, as shown in Figure 2a, the $FAPbI_3$-rich compositions have a broad PL peak and are shifted toward lower wavelengths. On the basis of this PL behavior and the yellow color of the microcrystals upon application of the antisolvent (Figure S1), we assume that the photoinactive, yellow phase (δ-$FAPbI_3$) has formed in combination with the black phase (α-$FAPbI_3$). Further, as shown in Figure 2a, the formation of this yellow phase begins to recede when the concentration of $MAPbI_3$ increases, confirming stabilization upon doping.[42] We also observe this phenomenon when chloroform is utilized as the antisolvent; however, as the peak intensities are low compared to the other spectra, it is not evident in Figure 2h. Shown in Figure S18 are the spectra of these compositions to confirm. From this initial measurement, we reach two conclusions: (1) neither toluene nor chloroform is the appropriate antisolvent choice for the formation of a pure phase α-$FAPbI_3$ and (2) stabilization of the α-$FAPbI_3$ phases can be achieved through a small amount of $MAPbI_3$ in agreement with previous studies.[42]

Further, by exploring the time-dependent PL behavior, we conclude this double cation system undergoes fewer changes in PL spectra over time when toluene is utilized as the antisolvent instead of chloroform. As mentioned previously, the $FAPbI_3$-rich compositions are likely a solid solution between the δ-$FAPbI_3$ and α-$FAPbI_3$ phases; therefore, when we examine the characteristic PL behaviors (Figure 2e,l) and corresponding loading maps (Figure 2b,i) when either toluene or chloroform is used, we observe a broad peak at lower wavelengths spanning approximately 100 nm. With using chloroform, this peak disappears quickly after roughly 30 min, whereas with the toluene system, we see this peak begin to narrow and shift toward lower wavelengths, indicating the continued presence of these mixed phases in toluene rather than in chloroform. Next, we observe a similar trend when comparing the solid solution between $FAPbI_3$-rich and $MAPbI_3$ compositions in toluene and chloroform. Even with a small peak shift and slight decrease in intensity, toluene as the antisolvent produces a consistent PL peak for the entirety of the characterization (roughly 6 h in ambient conditions), as shown in Figure 2c,f. Other studies have confirmed that the stabilization of α-$FAPbI_3$ in ambient conditions can be achieved through small amounts of alloying with $MAPbI_3$.[42] Conversely, this stabilization is temporary when chloroform is used as the antisolvent, as shown in Figure 2j,m. For approximately 4 h, we observe a steady PL peak before it begins to vanish. We attribute this decrease in PL intensity to the perovskite reacting with the moisture in ambient conditions, possibly causing the sample to revert to PbI_2 or forming a hydrate product.[43] Our conclusion that toluene is a better choice for this system is further confirmed by analyzing the time-dependent PL behavior of the $MAPbI_3$-rich compositions. As shown in Figure 2d,g, these compositions demonstrate remarkable stability as their peak properties, such as position and width, remain constant throughout the characterization even after a small increase in PL intensity at the beginning, indicating possible filling of trap states.[44] A similar increase in PL intensity is observed for the system when chloroform is used, as shown in Figure 2k,n; however, after approximately 5 h, the PL intensity decreases, indicating the formation of hydrate products is occurring for these samples as well.[43]

It has been well-established that the combination of MA and FA cations can stabilize the cubic perovskite phase and deter the degradation of the perovskite.[45−47] One systematic investigation performed by Charles et al. details the routes and kinetics in which this system degrades under dry atmospheric conditions.[48] MA-rich phases decompose into MAI and PbI_2, while FA-rich phases transform into the yellow, photoinactive phase, δ-$FAPbI_3$. Conversely, mixed cation phases ($0.4 \leq x \leq 0.6$) demonstrate remarkable stability as the degradation route to the end-members is less thermodynamically favorable. Here, we find a broader compositional

https://doi.org/10.1021/jacs.1c10045
J. Am. Chem. Soc. 2021, 143, 19945−19955

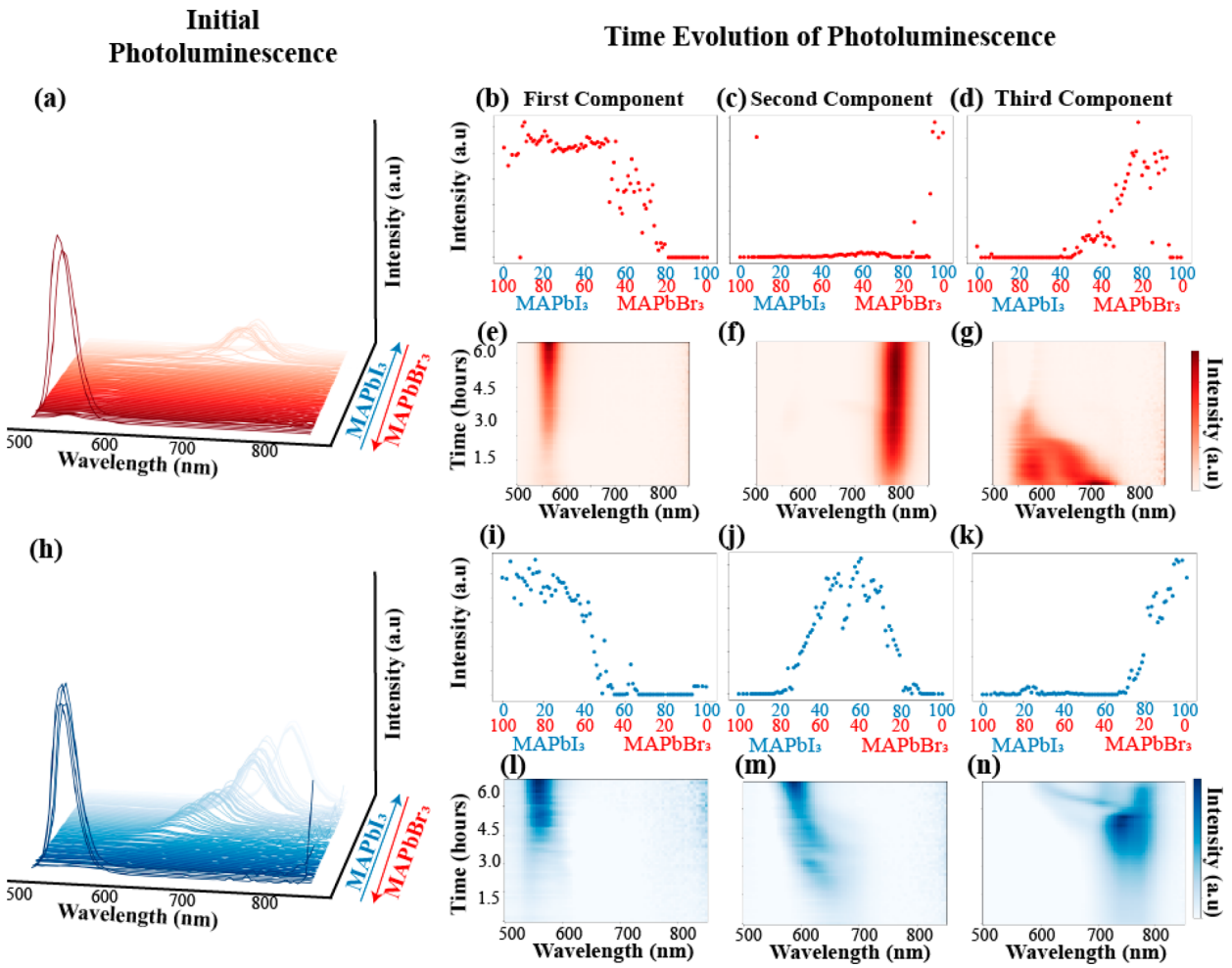

Figure 3. Methylammonium lead double halide system, $MAPb(I_xBr_{1-x})_3$. (a) Initial PL behavior when toluene is used as the antisolvent. (b−d) Loading maps for (b) $MAPbBr_3$-rich compositions, (c) solid solutions of $MAPbBr_3$ and $MAPI_3$, and (d) $MAPbI_3$-rich compositions, respectively. (e−g) Characteristic PL behaviors for (e) $MAPbBr_3$-rich compositions, (f) solution solutions of $MAPbBr_3$ and $MAPbI_3$, and (g) $MAPbI_3$-rich compositions, respectively. (h) Initial PL behavior when chloroform is used as the antisolvent. Similar to NMF decomposition for the toluene data set (i)−(k) and (l)−(n) are the (i, j, k) loading maps and (l, m, n) characteristic PL behaviors for $MAPbBr_3$-rich compositions, solution solutions of $MAPbBr_3$ and $MAPbI_3$, and $MAPbI_3$-rich compositions, respectively.

region $(0 \leq x \leq 0.9)$ to not exhibit changes in PL behavior indicating degradation. This improved stability could be attributed to the utilization of antisolvent as the study by Charles et al. does not use an antisolvent in their fabrication. We explored this system further by performing the same synthesis and characterization of this system but utilized chlorobenzene as the antisolvent. Chlorobenzene falls into the same category as chloroform, a halogenated antisolvent but includes an aromatic comp. Other studies have widely utilized this antisolvent to improve the performance.[49,50] The initial and time- and composition-dependent PL behavior of the system is compared to the behavior when toluene and chloroform are used and shown in Figures S3−S6. We postulate that these differences in PL behavior between the two groups are caused by the antisolvent's ability in dissociating the coordinative bonds between the solvent and Pb ion. We suggest that the presence of the halogenated ion in the antisolvent does not fully cause this dissociation and, therefore, cause complex lead halide ions, such as $[PbI_3]^-$, to remain, interact with air, and motivate degradation.

Next, we further proceed by investigating how the change in antisolvent affects a mixed halide perovskite system, $MAPb(I_xBr_{1-x})_3$. As shown in Figure 3a,h, we observe a peak shift toward higher wavelengths as the concentration of $MAPbI_3$ increases, indicating an expected decrease in the band gap. This shift is more apparent when chloroform is utilized as the antisolvent as the $MAPbI_3$-rich compositions have comparatively a large PL intensity as compared to the same compositions when toluene was used.

Regardless of the antisolvent, the PL behavior of $MAPbBr_3$-rich compositions is approximately the same; however, this is not applicable as more $MAPbI_3$ is introduced into the system. For $MAPbBr_3$-rich compositions, we observe an increase in PL intensity without any shift in peak position for both toluene (Figure 3b,e) and chloroform (Figure 3i,l), indicating that these compositions are stable regardless of antisolvent choice. Solid solutions between $MAPbBr_3$ and $MAPbI_3$ experience two different dynamical processes depending on the antisolvent used during synthesis. For example, as shown in Figure 3c,f, a broad peak, likely indicative of two convolved peaks, is present initially. This peak begins to separate into two, with one representing the bromine-rich phase and one the mixed phase. After approximately 3 h, both peaks disappear, indicating complete degradation of the compositions. Simultaneously,

https://doi.org/10.1021/jacs.1c10045
J. Am. Chem. Soc. 2021, 143, 19945−19955

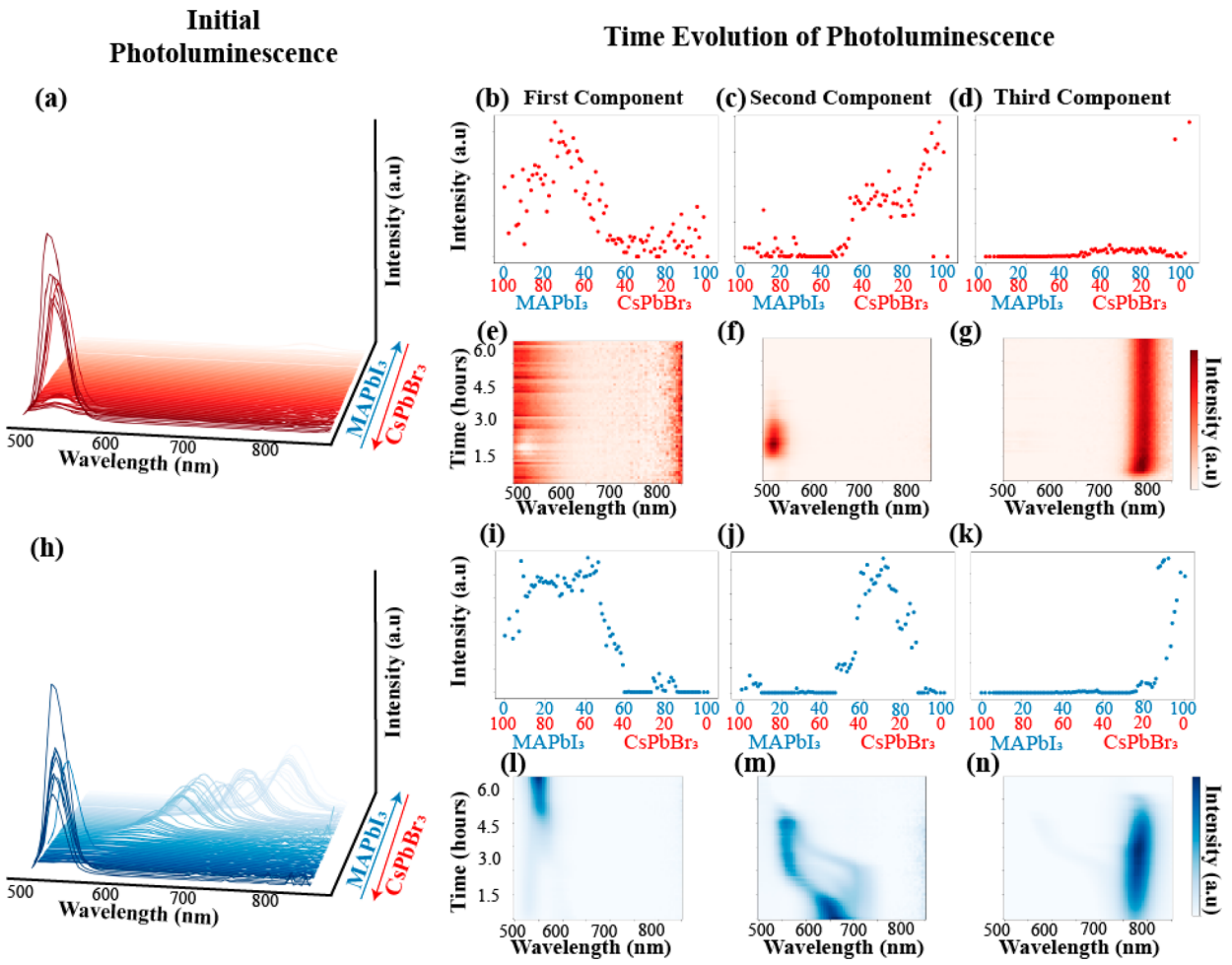

Figure 4. Double cation and double halide system, $MA_xCs_{1-x}Pb(I_xBr_{1-x})_3$. (a) Initial PL behavior when toluene is used as the antisolvent. (b–d) Loading maps for (b) $CsPbBr_3$-rich compositions, (c) solution solutions of $CsPbBr_3$ and $MAPbI_3$, and (d) $MAPbI_3$-rich compositions, respectively. (e–g) Characteristic PL behaviors for (e) $CsPbBr_3$-rich compositions, (f) solution solutions of $CsPbBr_3$ and $MAPbI_3$, and (g) $MAPbI_3$-rich compositions, respectively. (h) Initial PL behavior when chloroform is used as the antisolvent. Similar to NMF decomposition for the toluene data set (i)–(k) and (l)–(n) are the (i, j, k) loading maps and (l, m, n) characteristic PL behaviors for $CsPbBr_3$-rich compositions, solution solutions of $CsPbBr_3$, and $MAPbI_3$, and $MAPbI_3$-rich compositions, respectively.

when these same compositions are synthesized using chloroform as the antisolvent, we observe the presence of a broad, low-intensity peak, as shown in Figure 3j,m. Over time, it appears to narrow as the intensity of the bromine-rich phase increases and the mixed phase decreases. In both cases, we observe halide segregation caused by reactions with the environment,[37] indicating that halide segregation cannot be prevented for these particular composition ranges using these two antisolvents. Finally, $MAPbI_3$-rich compositions in this system behave similarly to the same region of the phase diagram for the $MA_xFA_xPbI_3$, as expected. As shown in Figure 3d,g, the $MAPbI_3$-rich compositions, specifically $x \leq 10\%$, experience an increase in PL intensity but remain stable for the entirety of the experiment when toluene is utilized. As with the $MAPbI_3$-rich compositions when chloroform is used, we observe an increase and subsequent decrease in PL intensity as they are exposed to air, as shown in Figure 3k,n. Interestingly, we observe a small peak extending toward lower wavelengths, indicating halide segregation occurring even with a small amount of $MAPbBr_3$ when chloroform is used.

Overall, this system typically undergoes halide segregation when exposed to ambient conditions, and we observe that neither antisolvent mitigates this phenomenon. It has been demonstrated that alloying with small amounts of $MAPbBr_3$ (<10%) in $MAPbI_3$ can increase stability where toluene is used as the antisolvent,[51] and we observe this as well. Conversely, we do not observe this improvement in stability when chloroform is utilized as the antisolvent. We credit the improvements in stability because of toluene over chloroform for the same reasons suggested regarding the $MA_xFA_{1-x}PbI_3$ system.

We proceed further by investigating the effect of each antisolvent on the double cation and double halide system, $MA_xCs_{1-x}Pb(I_xBr_{1-x})_3$, as shown in Figure 4. As mentioned previously, we compare this system to a similar one which uses different precursors, $MA_xCs_{1-x}Pb(Br_xI_{1-x})_3$ (Figure 5). First, as shown in Figure 4a,h, we clearly observe that $MAPbI_3$-rich compositions are comparatively lower in intensity than $CsPbBr_3$-rich compositions when toluene is used, whereas this is not the case when chloroform is utilized as we can see high-intensity $MAPbI_3$ peaks. However, in both cases, adherence to Vegard's law, in which the band gap shifts based on compositional alloying, is upheld.

Regarding the time-dependent PL behavior, from the NMF decompositions, it becomes apparent that toluene is a more

https://doi.org/10.1021/jacs.1c10045
J. Am. Chem. Soc. 2021, 143, 19945–19955

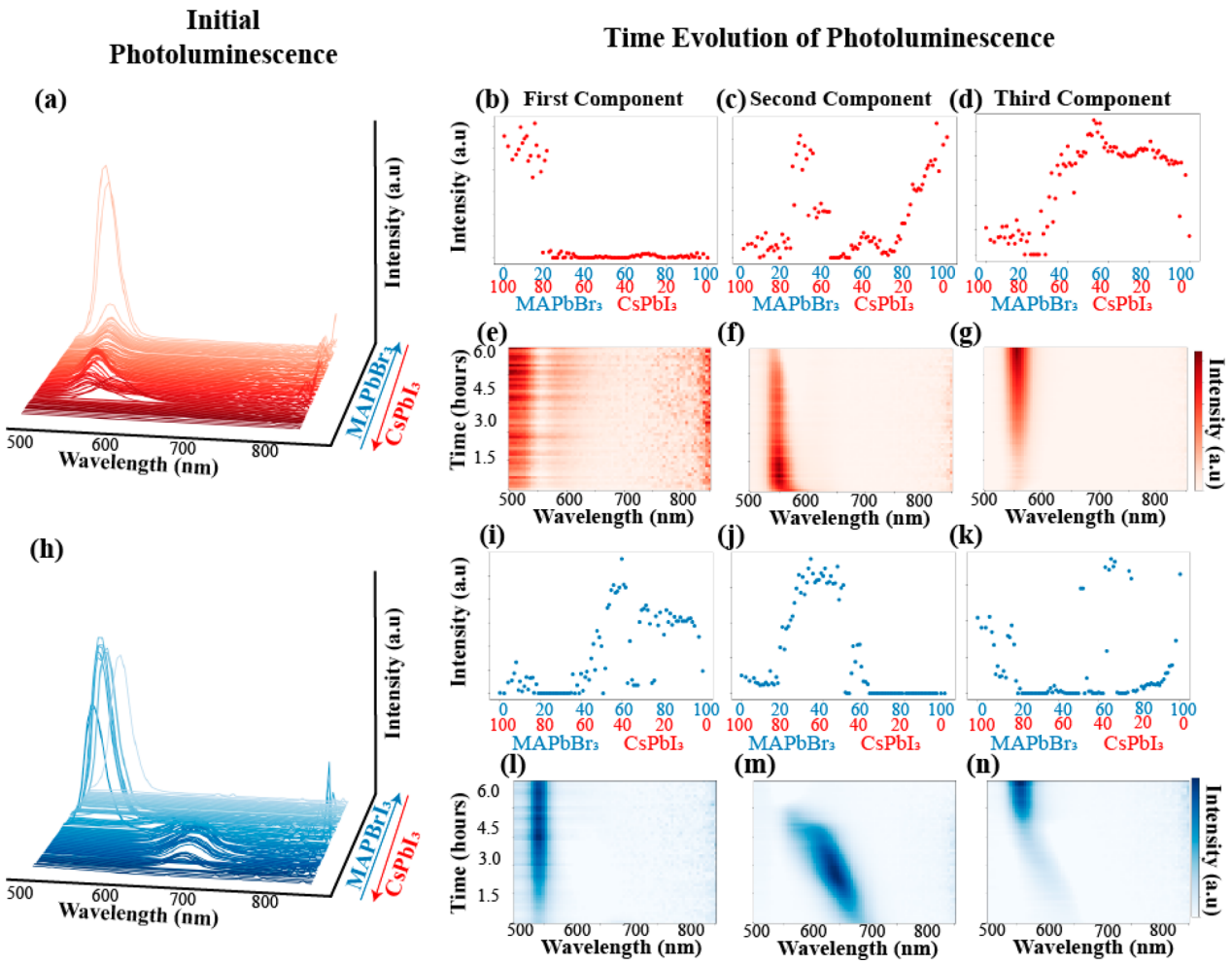

Figure 5. Double cation and double halide system, $MA_xCs_{1-x}Pb(Br_xI_{1-x})_3$. (a) Initial PL behavior when toluene is used as the antisolvent. (b−d) Loading maps for (b) $CsPbI_3$-rich compositions, (c) solution solutions of $CsPbI_3$ and $MAPbBr_3$, and (d) $MAPbBr_3$-rich compositions, respectively. (e−g) Characteristic PL behaviors for (e) $CsPbI_3$-rich compositions, (f) solution solutions of $CsPbI_3$ and $MAPbBr_3$, and (g) $MAPbBr_3$-rich compositions, respectively. (h) Initial PL behavior when chloroform is used as the antisolvent. Similar to NMF decomposition for the toluene data set (i)−(k) and (l)−(n) are the (i, j, k) loading maps and (l, m, n) characteristic PL behaviors for $CsPbI_3$-rich compositions, solution solutions of $CsPbI_3$ and $MAPbBr_3$, and $MAPbBr_3$-rich compositions, respectively.

beneficial antisolvent for $MAPbI_3$ and chloroform is a better antisolvent for $CsPbBr_3$. As shown in Figure 4b,e, rapid degradation of the $CsPbBr_3$-rich compositions is observed when toluene is used because the individual PL spectra could simply be characterized as noise, as shown in Figure S19. Conversely, when chloroform is utilized as the antisolvent, for these same compositions, we observe an increase in peak intensity without major peak shifts, indicating the stability of these compositions over 6 h in ambient conditions, as shown in Figure 4i,l. Next, we explore how each antisolvent affected the stability of solid solutions of $MAPbI_3$-rich compositions and $CsPbBr_3$. For toluene, we observe a brief appearance of an intense peak after approximately 2 h before it disappears, as shown in Figure 4c,f. Noticeably, even though these compositions contain a considerable amount of iodide, we do not observe an iodide-rich-phase PL peak. On the contrary, when chloroform is used, we initially observe a mixed-phase PL peak, as shown in Figure 4j,m; however, after approximately 2 h, this peak separates into two peaks, each representing the iodide-rich and bromide-rich phases, confirming halide segregation.[37] Interestingly, the $MAPbI_3$-rich peak appears not to disappear as time increases but begins to shift toward lower wavelengths. Finally, as stated previously, $MAPbI_3$-rich compositions are remarkably stable with toluene as the antisolvent, as shown in Figure 4d,g, whereas when chloroform is used, these same compositions experience an increase in PL intensity before another decrease, as shown in Figure 4k,n. Overall, it was not unexpected that for $CsPbBr_3$-rich compositions, toluene is not the appropriate antisolvent choice because of the polarity index disparity between DMSO and toluene.[52]

Further, we explore a system similar to that of Figure 4 by utilizing different precursors to analyze the PL behavior of the system: $MA_xCs_{1-x}Pb(Br_xI_{1-x})_3$. When either toluene or chloroform is utilized, the initial PL behavior for $MAPbBr_3$-rich compositions is a well-defined, high-intensity peak, as shown in Figure 5a,h. For $CsPbI_3$-rich compositions, there is a broad low-intensity peak observed when toluene is used, as shown in Figure S20a, indicating this material formed not only the black phase of $CsPbI_3$ but also the wide-band-gap, polymorph δ-$CsPbI_3$.[53] The formation of this phase is not dependent on the antisolvent, as evidenced by its presence when chloroform is used, as shown in Figure S20b. Noticeably,

https://doi.org/10.1021/jacs.1c10045
J. Am. Chem. Soc. 2021, 143, 19945−19955

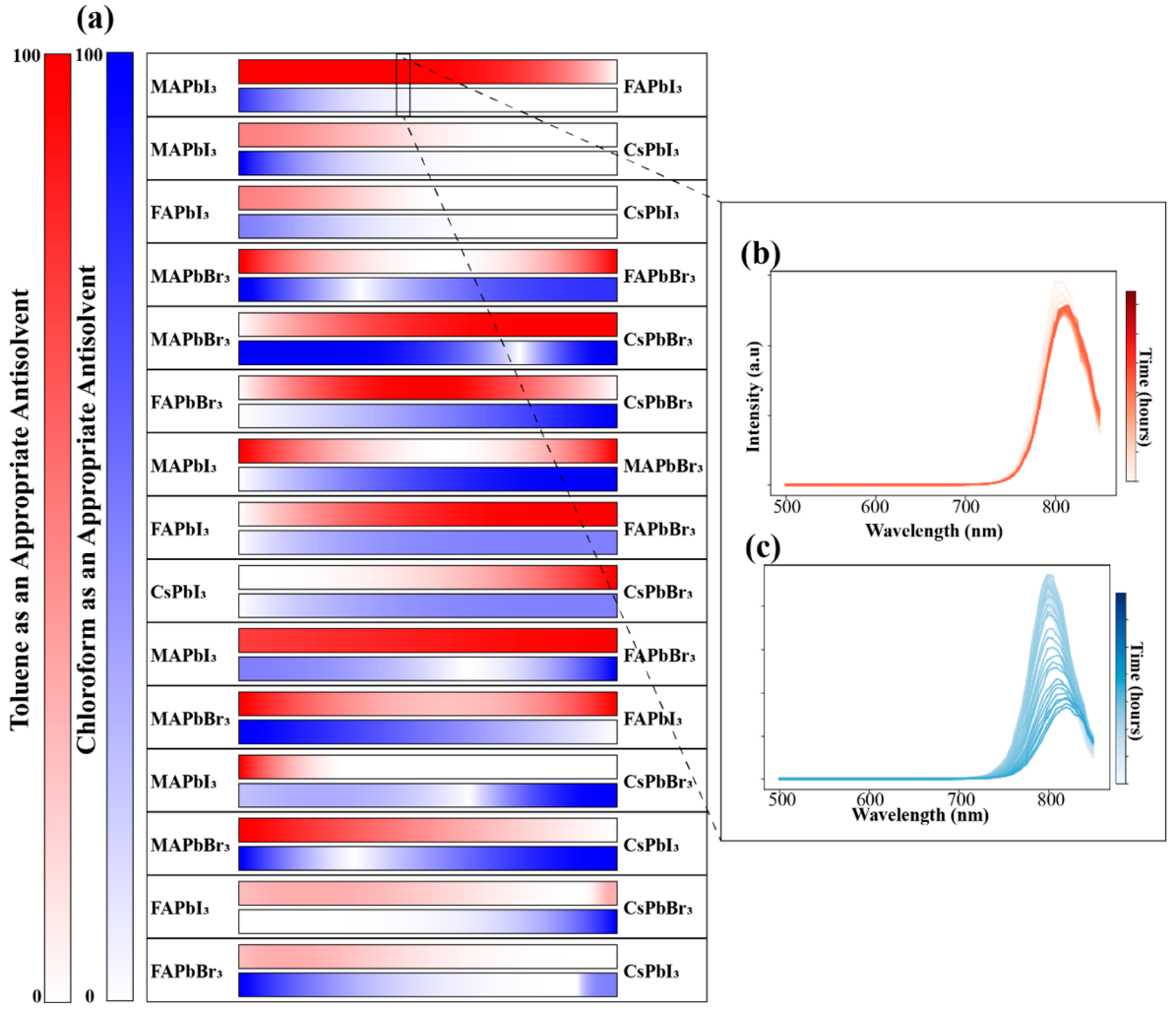

Figure 6. Guide for which antisolvent is more applicable for each binary MHP system. (a) White or light red/blue indicates the antisolvent is not ideal for that section of the phase diagram as the microcrystals either form different phases or exhibit poor stability. As the color darkens, this indicates the antisolvent is an appropriate choice for the portion of the phase diagram as the correct phase forms and remains stable for longer periods of time. (b) Relatively consistent PL spectrum when toluene is used. (c) Changing PL spectrum, including a peak shift and decrease in intensity, when chloroform is utilized.

Vegard's law is better adhered to when chloroform is utilized versus the usage of toluene.

Regarding the time-dependent evolution of the PL for this system, we observe a variety of dynamical processes caused by either antisolvent. First, the formation of $CsPbI_3$, most likely the polymorph phases, when toluene is used produces an unstable composition, as evidenced by Figure 5b,e. Surprisingly, chloroform produces a stable, yellow phase δ-$CsPbI_3$, as shown in Figure 5i,l. The band gap of this polymorph is roughly 2.82 eV,[53] explaining the apparent peak at lower wavelengths, shown in Figure 5l. Next, solid solutions between $CsPbI_3$-rich and $MAPbBr_3$ compositions exhibit a decreasing PL intensity at one peak wavelength over the course of time, indicating degradation of the compositions, as shown in Figure 5c,f. Conversely, these same compositions begin with a single mixed-phase PL peak before experiencing halide segregation as the peak begins to move toward lower wavelengths, as shown in Figure 5j,m. Finally, we observe similar trends, in which the peak grows in intensity of time, for the $MAPbBr_3$-rich compositions for both antisolvents (Figure 5d,g,k,n). However, as shown in Figure 5k, when chloroform is used, these compositions also include fair amounts of $CsPbI_3$, explaining the peak shift over time, as shown in Figure 5n. Full stability analysis of this system is limited by the formation of δ-$CsPbI_3$ as it does not allow us to fully explore dynamical processes, such as halide segregation, when toluene is used; however, chloroform appears to be the appropriate choice to help with the formation of α-$CsPbI_3$ through alloying with $MAPbBr_3$.

Finally, we compare the solid solutions of the system $MA_xCs_{1-x}Pb(I_xBr_{1-x})_3$ and the system $MA_xCs_{1-x}Pb(Br_xI_{1-x})_3$ to compare the effect of the precursors as related to the antisolvent choice. To clarify, in the system $MA_xCs_{1-x}Pb(I_xBr_{1-x})_3$ $MAPbI_3$ and $CsPbBr_3$ are the stock precursors, while in the system $MA_xCs_{1-x}Pb(Br_xI_{1-x})_3$ the precursors are $MAPbBr_3$ and $CsPbI_3$. For both systems, it is demonstrated that toluene is not the appropriate choice for solid solutions of $CsPbX_3$-rich compositions and $MAPbX_3$. In the $MA_xCs_{1-x}Pb(I_xBr_{1-x})_3$ system, the polar index disparity between DMSO and toluene causes the formation of $CsPbBr_3$ to be stagnated, whereas toluene produces an unstable δ-$CsPbI_3$ phase in the $MA_xCs_{1-x}Pb(Br_xI_{1-x})_3$ system. Conversely, in both systems, chloroform produces initial mixed-phase compositions; however, eventually, halide segregation begins to occur. Overall, this comparison is indicative of the precursor having an effect

https://doi.org/10.1021/jacs.1c10045
J. Am. Chem. Soc. 2021, 143, 19945−19955

on the types of dynamical processes that occur as caused by the solvent in which the end-member is dissolved.

Finally, through the examination of the NMF decompositions of each binary system, we produce Figure 6a as a guide for which antisolvent produces a more intrinsically stable perovskite with a particular composition. As mentioned previously, this stability is determined by a consistent PL spectrum over time, in which the peak intensity remains relatively constant, the peak position does not drastically shift, or a secondary peak does not appear. Therefore, if the composition is stable with a particular antisolvent, it is represented with a dark color, whereas, if those changes are observed, a light color is used to indicate that it is not the appropriate antisolvent for stability. For example, toluene is considered a more appropriate choice of antisolvent, as indicated by the dark red color in the guide, because the PL spectrum remains relatively unchanged over time, as shown in Figure 6b. This is not observed when chloroform is utilized for the same composition, as indicated by a peak shift toward lower wavelengths and decrease in peak intensity (Figure 6c). Here, we also highlight the remarkable stability in ambient conditions for microcrystals of $MAPbI_3$-rich compositions and solid solutions between $FAPbI_3$-rich and $MAPbI_3$ compositions when toluene is utilized.

In summary, we have demonstrated the effect of antisolvents on the initial photoluminescence behavior for multicomponent MHPs and on the dynamical processes experienced by these compositions over time when exposed to ambient conditions. Noticeably, through this study, when toluene is utilized as the antisolvent, we observe improved stability in a broad compositional region of the $MA_xFA_{1-x}PbI_3$ system previously thought unstable. Although our measurements were on microcrystals, these results can also be confirmed by results in the literature. For example, Liu et al. observed a bimodal distribution of band gaps in $Cs_xMA_{1-x}PbBr_3$ single crystals utilizing PL measurements.[54] We observe a similar trend in PL behavior, as shown in Figure S21, for the same system, further validating our results. We demonstrate how these workflows are beneficial to determining the intrinsic stability of a composition, which is a crucial step in developing a stable and efficient device for applications.

We postulate such drastic differences in stability are caused by the relative solubility of the precursor components in each antisolvent.[55] Simplistically, as the antisolvent is added to the precursor solution, it extracts the antisolvent, triggering nucleation of the perovskite material. The overall effectiveness of an antisolvent is determined by the differences between the precursor material and the solvent. For example, if the antisolvent removes the organic halides upon application along with the solvent, residual PbX_2 remains in the precursor solution, leading to further degradation upon exposure to ambient conditions. Overall, we highlight how we cannot simply utilize a standard recipe for the processing of different MHPs, emphasizing the importance of antisolvent engineering in intrinsic stability.

CONCLUSION

Through the utilization of our previously reported workflow,[29] we have demonstrated how it can be used to synthesize and characterize large amounts of compositions using two different antisolvents to explore both the effect of experimental choices and dynamical processes caused by exposure to ambient conditions. As stated previously, we synthesized and characterized approximately 2880 different microcrystal samples of 15 different binary mixed cation and mixed halide perovskite systems. Altogether the absolute synthesis and characterization times total only 1.5 weeks. We observed drastically different PL spectra evolutions in ambient conditions of the same perovskite compositions, entirely dependent on the antisolvent utilized. We conclude which antisolvent is the appropriate choice for a particular compositional region based on the characteristic PL spectrum, providing guidance for future studies to explore the exact intricacies of the intrinsic material stability of a specific composition.

ASSOCIATED CONTENT

Supporting Information

The Supporting Information is available free of charge at https://pubs.acs.org/doi/10.1021/jacs.1c10045.

Robotic synthesis, automated PL characterization, and NMF; time- and composition-dependent PL behavior of the other 11 binary systems mentioned (PDF)

AUTHOR INFORMATION

Corresponding Author

Mahshid Ahmadi − *Institute for Advanced Materials and Manufacturing, Department of Materials Science and Engineering, The University of Tennessee Knoxville, Knoxville, Tennessee 37996, United States;* orcid.org/0000-0002-3268-7957; Email: mahmadi3@utk.edu

Authors

Kate Higgins − *Institute for Advanced Materials and Manufacturing, Department of Materials Science and Engineering, The University of Tennessee Knoxville, Knoxville, Tennessee 37996, United States;* orcid.org/0000-0001-5503-2884

Maxim Ziatdinov − *Center for Nanophase Materials Sciences and Computational Sciences and Engineering Division, Oak Ridge National Laboratory, Oak Ridge, Tennessee 37831, United States;* orcid.org/0000-0003-2570-4592

Sergei V. Kalinin − *Center for Nanophase Materials Sciences, Oak Ridge National Laboratory, Oak Ridge, Tennessee 37831, United States;* orcid.org/0000-0001-5354-6152

Complete contact information is available at: https://pubs.acs.org/10.1021/jacs.1c10045

Notes

The authors declare no competing financial interest.

ACKNOWLEDGMENTS

This research was supported by the National Science Foundation (NSF), Award No. 2043205, and the StART UTK−ORNL science alliance program. M.A. and K.H. acknowledge support from CNMS user facility, Project No. CNMS2021-B-00922. K.H. was partially supported by the Center for Materials Processing, a Center of Excellence at the University of Tennessee Knoxville, funded by the Tennessee Higher Education Commission (THEC). The machine learning process development (M.Z., S.V.K.) was supported by the Oak Ridge National Laboratory's Center for Nanophase Materials Sciences, which is a U.S. DOE Office of Science User Facility.

REFERENCES

(1) Park, N.-G.; Grätzel, M.; Miyasaka, T.; Zhu, K.; Emery, K. Towards stable and commercially available perovskite solar cells. *Nature Energy* **2016**, *1* (11), 16152.

(2) Ahmadi, M.; Wu, T.; Hu, B. A Review on Organic-Inorganic Halide Perovskite Photodetectors: Device Engineering and Fundamental Physics. *Adv. Mater.* **2017**, *29* (41), 1605242.

(3) Lukosi, E.; Smith, T.; Tisdale, J.; Hamm, D.; Seal, C.; Hu, B.; Ahmadi, M. Methylammonium lead tribromide semiconductors: Ionizing radiation detection and electronic properties. *Nucl. Instrum. Methods Phys. Res., Sect. A* **2019**, *927*, 401−406.

(4) Shrestha, S.; Fischer, R.; Matt, G. J.; Feldner, P.; Michel, T.; Osvet, A.; Levchuk, I.; Merle, B.; Golkar, S.; Chen, H.; Tedde, S. F.; Schmidt, O.; Hock, R.; Rührig, M.; Göken, M.; Heiss, W.; Anton, G.; Brabec, C. J. High-performance direct conversion X-ray detectors based on sintered hybrid lead triiodide perovskite wafers. *Nat. Photonics* **2017**, *11* (7), 436−440.

(5) Zhao, B.; Bai, S.; Kim, V.; Lamboll, R.; Shivanna, R.; Auras, F.; Richter, J. M.; Yang, L.; Dai, L.; Alsari, M.; She, X.-J.; Liang, L.; Zhang, J.; Lilliu, S.; Gao, P.; Snaith, H. J.; Wang, J.; Greenham, N. C.; Friend, R. H.; Di, D. High-efficiency perovskite−polymer bulk heterostructure light-emitting diodes. *Nat. Photonics* **2018**, *12* (12), 783−789.

(6) Zou, Y.; Yuan, Z.; Bai, S.; Gao, F.; Sun, B. Recent progress toward perovskite light-emitting diodes with enhanced spectral and operational stability. *Materials Today Nano* **2019**, *5*, 100028.

(7) Liu, W. W.; Wu, T. H.; Liu, M. C.; Niu, W. J.; Chueh, Y. L. Recent Challenges in Perovskite Solar Cells Toward Enhanced Stability, Less Toxicity, and Large-Area Mass Production. *Adv. Mater. Interfaces* **2019**, *6* (9), 1801758.

(8) Salhi, B.; Wudil, Y. S.; Hossain, M. K.; Al-Ahmed, A.; Al-Sulaiman, F. A. Review of recent developments and persistent challenges in stability of perovskite solar cells. *Renewable Sustainable Energy Rev.* **2018**, *90*, 210−222.

(9) Hwang, I.; Jeong, I.; Lee, J.; Ko, M. J.; Yong, K. Enhancing Stability of Perovskite Solar Cells to Moisture by the Facile Hydrophobic Passivation. *ACS Appl. Mater. Interfaces* **2015**, *7* (31), 17330−6.

(10) Lee, J.-W.; Kim, D.-H.; Kim, H.-S.; Seo, S.-W.; Cho, S. M.; Park, N.-G. Formamidinium and Cesium Hybridization for Photo- and Moisture-Stable Perovskite Solar Cell. *Adv. Energy Mater.* **2015**, *5* (20), 1501310.

(11) Seo, S.; Jeong, S.; Bae, C.; Park, N. G.; Shin, H. Perovskite Solar Cells with Inorganic Electron- and Hole-Transport Layers Exhibiting Long-Term (approximately 500 h) Stability at 85 degrees C under Continuous 1 Sun Illumination in Ambient Air. *Adv. Mater.* **2018**, *30*, 1801010.

(12) Xu, F.; Zhang, T.; Li, G.; Zhao, Y. Mixed cation hybrid lead halide perovskites with enhanced performance and stability. *J. Mater. Chem. A* **2017**, *5* (23), 11450−11461.

(13) Hieulle, J.; Wang, X.; Stecker, C.; Son, D. Y.; Qiu, L.; Ohmann, R.; Ono, L. K.; Mugarza, A.; Yan, Y.; Qi, Y. Unraveling the Impact of Halide Mixing on Perovskite Stability. *J. Am. Chem. Soc.* **2019**, *141* (8), 3515−3523.

(14) McMeekin, D. P.; Rehman, W.; Eperon, G. E.; Saliba, M.; Hörantner, M. T.; Haghighirad, A.; Sakai, N.; Korte, L.; Rech, B.; Johnston, M. B.; Herz, L. M.; Snaith, H. J.; Sadoughi, G. A Mixed-Cation Lead Mixed-Halide Perovskite Absorber for Tandem Solar Cells. *Science* **2016**, *351* (6269), 151−155.

(15) Saliba, M.; Matsui, T.; Seo, J. Y.; Domanski, K.; Correa-Baena, J. P.; Nazeeruddin, M. K.; Zakeeruddin, S. M.; Tress, W.; Abate, A.; Hagfeldt, A.; Gratzel, M. Cesium-containing triple cation perovskite solar cells: improved stability, reproducibility and high efficiency. *Energy Environ. Sci.* **2016**, *9* (6), 1989−1997.

(16) Li, W.-G.; Rao, H.-S.; Chen, B.-X.; Wang, X.-D.; Kuang, D.-B. A formamidinium−methylammonium lead iodide perovskite single crystal exhibiting exceptional optoelectronic properties and long-term stability. *J. Mater. Chem. A* **2017**, *5* (36), 19431−19438.

(17) Jeon, N. J.; Noh, J. H.; Kim, Y. C.; Yang, W. S.; Ryu, S.; Seok, S. I. Solvent engineering for high-performance inorganic-organic hybrid perovskite solar cells. *Nat. Mater.* **2014**, *13* (9), 897−903.

(18) Shi, D.; Adinolfi, V.; Comin, R.; Yuan, M.; Alarousu, E.; Buin, A.; Chen, Y.; Hoogland, S.; Rothenberger, A.; Katsiev, K.; Losovyj, Y.; Zhang, X.; Dowben, P. A.; Mohammed, O. F.; Sargent, E. H.; Bakr, O. M. Solar cells. Low trap-state density and long carrier diffusion in organolead trihalide perovskite single crystals. *Science* **2015**, *347* (6221), 519−22.

(19) Seth, S.; Samanta, A. A Facile Methodology for Engineering the Morphology of CsPbX3 Perovskite Nanocrystals under Ambient Condition. *Sci. Rep.* **2016**, *6*, 37693.

(20) Jung, M.; Ji, S. G.; Kim, G.; Seok, S. I. Perovskite precursor solution chemistry: from fundamentals to photovoltaic applications. *Chem. Soc. Rev.* **2019**, *48* (7), 2011−2038.

(21) Sakai, N.; Pathak, S.; Chen, H.-W.; Haghighirad, A. A.; Stranks, S. D.; Miyasaka, T.; Snaith, H. J. The mechanism of toluene-assisted crystallization of organic−inorganic perovskites for highly efficient solar cells. *J. Mater. Chem. A* **2016**, *4* (12), 4464−4471.

(22) Wang, Y.; Wu, J.; Zhang, P.; Liu, D.; Zhang, T.; Ji, L.; Gu, X.; David Chen, Z.; Li, S. Stitching triple cation perovskite by a mixed anti-solvent process for high performance perovskite solar cells. *Nano Energy* **2017**, *39*, 616−625.

(23) Epps, R. W.; Bowen, M. S.; Volk, A. A.; Abdel-Latif, K.; Han, S.; Reyes, K. G.; Amassian, A.; Abolhasani, M. Artificial Chemist: An Autonomous Quantum Dot Synthesis Bot. *Adv. Mater.* **2020**, *32* (30), 2001626.

(24) Gu, E.; Tang, X.; Langner, S.; Duchstein, P.; Zhao, Y.; Levchuk, I.; Kalancha, V.; Stubhan, T.; Hauch, J.; Egelhaaf, H. J.; Zahn, D.; Osvet, A.; Brabec, C. J. Robot-Based High-Throughput Screening of Antisolvents for Lead Halide Perovskites. *Joule* **2020**, *4* (8), 1806−1822.

(25) Choubisa, H.; Askerka, M.; Ryczko, K.; Voznyy, O.; Mills, K.; Tamblyn, I.; Sargent, E. H. Crystal Site Feature Embedding Enables Exploration of Large Chemical Spaces. *Matter* **2020**, *3* (2), 433−448.

(26) Li, Z.; Najeeb, M. A.; Alves, L.; Sherman, A. Z.; Shekar, V.; Cruz Parrilla, P.; Pendleton, I. M.; Wang, W.; Nega, P. W.; Zeller, M.; Schrier, J.; Norquist, A. J.; Chan, E. M. Robot-Accelerated Perovskite Investigation and Discovery. *Chem. Mater.* **2020**, *32* (13), 5650−5663.

(27) MacLeod, B. P.; Morrissey, T. D.; Häse, F.; Roch, L. M.; Dettelbach, E.; Moreira, R.; Yunker, L. P. E.; Rooney, M. B.; Deeth, J. R.; Lai, V.; Ng, G. J.; Situ, H.; Zhang, R. H.; Elliott, M. S.; Haley, T. H.; Dvorak, D. J.; Aspuru-Guzik, A.; Hein, J. E.; Berlinguette, C. P.; Parlane, F. G. L. Self-driving laboratory for accelerated discovery of thin-film materials. *Sci. Adv.* **2020**, *6*, eaaz8867.

(28) Li, J.; Lu, Y.; Xu, Y.; Liu, C.; Tu, Y.; Ye, S.; Liu, H.; Xie, Y.; Qian, H.; Zhu, X. AIR-Chem: Authentic Intelligent Robotics for Chemistry. *J. Phys. Chem. A* **2018**, *122* (46), 9142−9148.

(29) Higgins, K.; Valleti, S. M.; Ziatdinov, M.; Kalinin, S. V.; Ahmadi, M. Chemical Robotics Enabled Exploration of Stability in Multicomponent Lead Halide Perovskites via Machine Learning. *ACS Energy Letters* **2020**, *5* (11), 3426−3436.

(30) Manion, J. G.; Proppe, A. H.; Hicks, G. E. J.; Sargent, E. H.; Seferos, D. S. High-Throughput Screening of Antisolvents for the Deposition of High-Quality Perovskite Thin Films. *ACS Appl. Mater. Interfaces* **2020**, *12* (23), 26026−26032.

(31) Chen, S.; Hou, Y.; Chen, H.; Tang, X.; Langner, S.; Li, N.; Stubhan, T.; Levchuk, I.; Gu, E.; Osvet, A.; Brabec, C. J. Exploring the Stability of Novel Wide Bandgap Perovskites by a Robot Based High Throughput Approach. *Adv. Energy Mater.* **2018**, *8* (6), 1701543.

(32) Hou; Scheiner, S.; McMeekin, D. P.; Wang, Z.; Li, N.; Chen, H.; Richter, M.; Levchuk, I.; Schrenker, N.; Stubhan, T.; Luechinger, N. A.; Hirsch, A.; Steinrück, H.-P.; Fink, R. H.; Halik, M.; Snaith, H. J.; Brabec, C. J.; Du, H.; Killian, M. S.; Spiecker, E.; Schmuki, P. A generatic interface to reduce the efficiency-stability-cost gap of perovskite cells. *Science* **2017**, *358* (6367), 1192−1197.

(33) Yavari, M.; Mazloum-Ardakani, M.; Gholipour, S.; Tavakoli, M. M.; Turren-Cruz, S.-H.; Taghavinia, N.; Grätzel, M.; Hagfeldt, A.;

https://doi.org/10.1021/jacs.1c10045
J. Am. Chem. Soc. 2021, 143, 19945−19955

Saliba, M. Greener, Nonhalogenated Solvent Systems for Highly Efficient Perovskite Solar Cells. *Adv. Energy Mater.* **2018**, *8* (21), 1800177.
(34) Ahn, N.; Son, D. Y.; Jang, I. H.; Kang, S. M.; Choi, M.; Park, N. G. Highly Reproducible Perovskite Solar Cells with Average Efficiency of 18.3% and Best Efficiency of 19.7% Fabricated via Lewis Base Adduct of Lead(II) Iodide. *J. Am. Chem. Soc.* **2015**, *137* (27), 8696−9.
(35) Yin, M.; Xie, F.; Chen, H.; Yang, X.; Ye, F.; Bi, E.; Wu, Y.; Cai, M.; Han, L. Annealing-free perovskite films by instant crystallization for efficient solar cells. *J. Mater. Chem. A* **2016**, *4* (22), 8548−8553.
(36) Babbe, F.; Sutter-Fella, C. M. Optical Absorption-Based In Situ Characterization of Halide Perovskites. *Adv. Energy Mater.* **2020**, *10* (26), 1903587.
(37) Knight, A. J.; Wright, A. D.; Patel, J. B.; McMeekin, D. P.; Snaith, H. J.; Johnston, M. B.; Herz, L. M. Electronic Traps and Phase Segregation in Lead Mixed-Halide Perovskite. *ACS Energy Letters* **2019**, *4* (1), 75−84.
(38) Ruan, S.; Surmiak, M.-A.; Ruan, Y.; McMeekin, D. P.; Ebendorff-Heidepriem, H.; Cheng, Y.-B.; Lu, J.; McNeill, C. R. Light induced degradation in mixed-halide perovskites. *J. Mater. Chem. C* **2019**, *7* (30), 9326−9334.
(39) Schelhas, L. T.; Li, Z.; Christians, J. A.; Goyal, A.; Kairys, P.; Harvey, S. P.; Kim, D. H.; Stone, K. H.; Luther, J. M.; Zhu, K.; Stevanovic, V.; Berry, J. J. Insights into operational stability and processing of halide perovskite active layers. *Energy Environ. Sci.* **2019**, *12* (4), 1341−1348.
(40) Pellet, N.; Teuscher, J.; Maier, J.; Grätzel, M. Transforming Hybrid Organic Inorganic Perovskites by Rapid Halide Exchange. *Chem. Mater.* **2015**, *27* (6), 2181−2188.
(41) Bush, K. A.; Frohna, K.; Prasanna, R.; Beal, R. E.; Leijtens, T.; Swifter, S. A.; McGehee, M. D. Compositional Engineering for Efficient Wide Band Gap Perovskites with Improved Stability to Photoinduced Phase Segregation. *ACS Energy Letters* **2018**, *3* (2), 428−435.
(42) Binek, A.; Hanusch, F. C.; Docampo, P.; Bein, T. Stabilization of the Trigonal High-Temperature Phase of Formamidinium Lead Iodide. *J. Phys. Chem. Lett.* **2015**, *6* (7), 1249−53.
(43) Christians, J. A.; Miranda Herrera, P. A.; Kamat, P. V. Transformation of the excited state and photovoltaic efficiency of CH3NH3PbI3 perovskite upon controlled exposure to humidified air. *J. Am. Chem. Soc.* **2015**, *137* (4), 1530−8.
(44) Stranks, S. D.; Burlakov, V. M.; Leijtens, T.; Ball, J. M.; Goriely, A.; Snaith, H. J. Recombination Kinetics in Organic-Inorganic Perovskites: Excitons, Free Charge, and Subgap States. *Phys. Rev. Appl.* **2014**, *2* (3), 034007.
(45) Huang, Y.; Li, L.; Liu, Z.; Jiao, H.; He, Y.; Wang, X.; Zhu, R.; Wang, D.; Sun, J.; Chen, Q.; Zhou, H. The intrinsic properties of FA(1−x)MAxPbI3 perovskite single crystals. *J. Mater. Chem. A* **2017**, *5* (18), 8537−8544.
(46) Rehman, W.; McMeekin, D. P.; Patel, J. B.; Milot, R. L.; Johnston, M. B.; Snaith, H. J.; Herz, L. M. Photovoltaic mixed-cation lead mixed-halide perovskites: links between crystallinity, photo-stability and electronic properties. *Energy Environ. Sci.* **2017**, *10* (1), 361−369.
(47) Zhang, Y.; Grancini, G.; Feng, Y.; Asiri, A. M.; Nazeeruddin, M. K. Optimization of Stable Quasi-Cubic FAxMA1−xPbI3 Perovskite Structure for Solar Cells with Efficiency beyond 20%. *ACS Energy Letters* **2017**, *2* (4), 802−806.
(48) Charles, B.; Dillon, J.; Weber, O. J.; Islam, M. S.; Weller, M. T. Understanding the stability of mixed A-cation lead iodide perovskites. *J. Mater. Chem. A* **2017**, *5* (43), 22495−22499.
(49) Hong, M. J.; Johnson, R. Y.; Labram, J. G. Impact of Moisture on Mobility in Methylammonium Lead Iodide and Formamidinium Lead Iodide. *J. Phys. Chem. Lett.* **2020**, *11* (13), 4976−4983.
(50) Yang, F.; Dong, L.; Jang, D.; Tam, K. C.; Zhang, K.; Li, N.; Guo, F.; Li, C.; Arrive, C.; Bertrand, M.; Brabec, C. J.; Egelhaaf, H. J. Fully Solution Processed Pure α-Phase Formamidinium Lead Iodide Perovskite Solar Cells for Scalable Production in Ambient Condition. *Adv. Energy Mater.* **2020**, *10* (42), 2001869.
(51) Ruess, R.; Benfer, F.; Bocher, F.; Stumpp, M.; Schlettwein, D. Stabilization of Organic-Inorganic Perovskite Layers by Partial Substitution of Iodide by Bromide in Methylammonium Lead Iodide. *ChemPhysChem* **2016**, *17* (10), 1505−11.
(52) Kerner, R. A.; Zhao, L.; Xiao, Z.; Rand, B. P. Ultrasmooth metal halide perovskite thin films via sol−gel processing. *J. Mater. Chem. A* **2016**, *4* (21), 8308−8315.
(53) Wang, B.; Novendra, N.; Navrotsky, A. Energetics, Structures, and Phase Transitions of Cubic and Orthorhombic Cesium Lead Iodide (CsPbI3) Polymorphs. *J. Am. Chem. Soc.* **2019**, *141* (37), 14501−14504.
(54) Liu, F.; Wang, F.; Hansen, K. R.; Zhu, X. Y. Bimodal Bandgaps in Mixed Cesium Methylammonium Lead Bromide Perovskite Single Crystals. *J. Phys. Chem. C* **2019**, *123* (23), 14865−14870.
(55) Taylor, A. D.; Sun, Q.; Goetz, K. P.; An, Q.; Schramm, T.; Hofstetter, Y.; Litterst, M.; Paulus, F.; Vaynzof, Y. A general approach to high-efficiency perovskite solar cells by any antisolvent. *Nat. Commun.* **2021**, *12* (1), 1878.

https://doi.org/10.1021/jacs.1c10045
J. Am. Chem. Soc. 2021, 143, 19945−19955